



Published in final edited form as:

*Front Biosci (Landmark Ed)*. 2022 March 16; 27(3): 99. doi:10.31083/j.fbl2703099.

## Deep learning quantification of vascular pharmacokinetic parameters in mouse brain tumor models

Chad A. Arledge<sup>1,†</sup>, Deeksha M. Sankepalle<sup>1,†</sup>, William N. Crowe<sup>1</sup>, Yang Liu<sup>1</sup>, Lulu Wang<sup>1</sup>, Dawen Zhao<sup>1,2,\*</sup>

<sup>1</sup>Department of Biomedical Engineering, Wake Forest School of Medicine, Winston-Salem, NC 27157, USA

<sup>2</sup>Department of Cancer Biology, Wake Forest School of Medicine, Winston-Salem, NC 27157, USA

### Abstract

**Background:** Dynamic contrast-enhanced (DCE) MRI is widely used to assess vascular perfusion and permeability in cancer. In small animal applications, conventional modeling of pharmacokinetic (PK) parameters from DCE MRI images is complex and time consuming. This study is aimed at developing a deep learning approach to fully automate the generation of kinetic parameter maps,  $K_{trans}$  (volume transfer coefficient) and  $V_p$  (blood plasma volume ratio), as a potential surrogate to conventional PK modeling in mouse brain tumor models based on DCE MRI.

**Methods:** Using a 7T MRI, DCE MRI was conducted in U87 glioma xenografts growing orthotopically in nude mice. Vascular permeability  $K_{trans}$  and  $V_p$  maps were generated using the classical Tofts model as well as the extended-Tofts model. These vascular permeability maps were then processed as target images to a twenty-four layer convolutional neural network (CNN). The CNN was trained on  $T_1$ -weighted DCE images as source images and designed with parallel dual pathways to capture multiscale features. Furthermore, we performed a transfer study of this glioma trained CNN on a breast cancer brain metastasis (BCBM) mouse model to assess the potential of the network for alternative brain tumors.

---

This is an open access article under the [CC BY 4.0 license](https://creativecommons.org/licenses/by/4.0/).

\*Correspondence: dawzhao@wakehealth.edu (Dawen Zhao).

†These authors contributed equally.

#### Author contributions

CAA, DMS, LW, and DZ conceived and designed the research study. CAA, DMS, WNC, YL, and LW performed the research. WNC performed small animal imaging. CAA and DMS developed the network and analyzed the data. YL, LW, and DZ helped supervise the project and provided critical feedback. CAA, DMS, WNC, and DZ wrote the manuscript. All authors contributed to editorial changes in the manuscript. All authors read and approved the final manuscript.

#### Ethics approval and consent to participate

All animal procedures performed were approved by the Wake Forest University Institutional Animal Care and Use Committee (A21-124 and A21-160).

#### Conflict of interest

The authors declare no conflict of interest.

#### Supplementary material

Supplementary material associated with this article can be found, in the online version, at <https://www.imrpress.com/journal/FBL/27/3/10.31083/j.fbl2703099>.

**Results:** Our data showed a good match for both Ktrans and Vp maps generated between the target PK parameter maps and the respective CNN maps for gliomas. Pixel-by-pixel analysis revealed intratumoral heterogeneous permeability, which was consistent between the CNN and PK models. The utility of the deep learning approach was further demonstrated in the transfer study of BCBM.

**Conclusions:** Because of its rapid and accurate estimation of vascular PK parameters directly from the DCE dynamic images without complex mathematical modeling, the deep learning approach can serve as an efficient tool to assess tumor vascular permeability to facilitate small animal brain tumor research.

### Keywords

convolutional neural network; dynamic contrast enhanced MRI; pharmacokinetic modeling; glioblastoma; breast cancer brain metastasis; vascular permeability parameters

---

## 1. Introduction

Glioblastoma multiforme (GBM) is the most common and lethal primary brain cancer. GBM is characterized by invasive tumor cell growth and extensive angiogenesis. Despite the development of highly angiogenic and leaky microvessels, many GBM cells grow by co-opting the pre-existing vessels, where the blood-brain barrier (BBB) may remain intact. Thus, the BBB disruption in GBM is markedly heterogeneous, which prevents therapeutic concentrations of chemotherapeutic agents from reaching the tumor in brain parenchyma [1–5].

MRI provides a noninvasive tool for acquiring information about the tumor microenvironment. Advancements in MR techniques have increased noninvasive access to a significant amount of useful information on cancer metabolism and tumor heterogeneity, ranging from spatial scaled to functional or metabolic imaging. Dynamic contrast-enhanced (DCE) MRI is a widely used technique for obtaining information of vascular perfusion and permeability [6–10]. A series of T<sub>1</sub>-weighted (T<sub>1</sub>-w) images is acquired before and after an i.v. bolus injection of gadolinium chelates to capture the transport of the contrast agent (CA) into and away from a tissue/region. By measuring dynamic changes in T<sub>1</sub>-w signal intensity (SI) as a function of time and applying pharmacokinetic (PK) modeling, exchange of the CA between the intravascular and extravascular extracellular space (EES) can be quantitatively estimated to extract several vascular perfusion/permeability parameters. These parameters include the volume transfer coefficient (Ktrans), flux rate constant (Kep), fractional volume of the blood plasma (Vp), and fractional volume of the EES (Ve) [6,7,11]. However, PK modeling of gadolinium in DCE MRI is complex. Various PK models have been established including the Brix model [12], the classical Tofts model [13,14], and the extended Tofts (Ex-Tofts) model [15]. The Tofts model is widely used to estimate Ktrans, Kep, and/or Ve. The Ex-Tofts model is an extension upon the Tofts model that takes into account the volume of contrast in the blood plasma, Vp, in addition to Ktrans, Kep and Ve.

PK mathematical models require knowledge of the arterial input function (AIF), which is an important variable for the modeling accuracy [16–20]. Lack of accurate measurement of

the AIF, also known as the vascular input function (VIF), represents a major disadvantage of current PK models as a small deviation in the AIF can markedly affect the estimation accuracy of kinetic parameters. Measurements of the AIF are additionally more difficult if not impossible in small animals on a case-by-case basis. Hence, a population-based averaged AIF from literature assuming a consistent value is implemented here to avoid poor AIF manual measurements leading to poor PK parameter accuracy. Population-based averaged AIFs have additionally been shown to improve the reproducibility of PK parameters [18,20]. Moreover, PK models are solely based on fitting pixel parameters to the CA concentration curves [21]. The pixel-wise model fitting is computationally demanding for a whole MR scan with thousands of pixels and thus is commonly time and memory consuming. Furthermore, manual identification of CA arrival during the dynamic scans as well as additional MRI acquisitions for  $T_1$  measurements are also required for accurate modeling of PK parameters when using PK models.

To address these limitations, we are seeking a machine learning approach for faster DCE parameter estimation without human bias. Machine learning has been increasingly used to power various research areas as it provides us with the ability to augment the knowledge and efforts of experts with a tool that can help to analyze data, and consequently make better predictions and decisions. Machine learning is commonly divided into two general forms, unsupervised and supervised learning. Unsupervised learning is concerned with understanding the internal structures of unlabeled data in a fully automated manner. Supervised learning requires training data to be manually labeled, where the algorithm learns from the labeled training data to predict the correct label for the unlabeled test data [22]. The model developed in this study is a supervised deep learning algorithm. Compared to the conventional machine learning methods, which require considerable research and design effort to capture higher-level features of the data, deep learning models learn data representations at various levels of abstraction automatically [23,24]. One such advanced deep learning algorithm used for images is the convolutional neural network (CNN).

Recent studies have sought implementation of deep learning to facilitate clinical PK parameter generation [25–27]. Nalepa *et al.* [26] have developed a clinical end-to-end DCE processing pipeline for brain tumors. However, this approach uses deep learning only for tumor segmentation and hence still requires conventional PK modeling. Choi *et al.* [25] implemented deep learning to improve the reliability of the AIF generation in astrocytomas to improve PK parameter accuracy; however, similar to Nalepa *et al.* [26], this approach still requires conventional PK modeling. In an effort to develop a possible surrogate to conventional PK modeling, Ulas *et al.* [27] have demonstrated the feasibility of implementation of deep learning for automatic PK parameter generation directly from  $T_1$ -w DCE images in stroke patients. These studies have highlighted the potential of deep learning to facilitate clinical PK parameter generation; however, to the best of our knowledge there have been no efforts to apply these approaches for small animal brain tumor studies. Similar to the methodology proposed by Ulas *et al.* [27], we have developed a deep learning-based CNN to directly estimate the vascular parameters in brain tumors derived from DCE MRI without conventional PK modeling aimed at facilitating small animal glioma research (Fig. 1, Supplementary Fig. 1). The developed CNN in this project contains two pathways to efficiently capture multiscale features. The local pathway of

the CNN extracts the details of local image regions in the filter window, whereas the global pathway focuses on determining the contextual and structural information. Due to its strong generalization ability, this deep learning algorithm shows increased robustness to signal noise and can suppress any non-consequential parameters. Moreover, this CNN method estimates the kinetic parameters directly from the SI curve of CA over time. This eliminates several intermediate steps including manual CA arrival identification, additional MRI acquisitions for  $T_1$  measurements, estimation of the AIF, and application of curve-fitting, thereby, accelerating the process and avoiding human bias (Fig. 1).

## 2. Materials and methods

### 2.1 Orthotopic GBM and breast cancer brain metastasis mouse models

All animal procedures performed were approved by the Wake Forest University Institutional Animal Care and Use Committee. Human glioblastoma U87 cells were cultured in Dulbecco's modified Eagle's medium (DMEM) with 10% FBS, 1% L-Glutamine, and 1% penicillin-streptomycin at 37 °C with 5% CO<sub>2</sub>. Once 80% confluence was achieved, the cells were harvested and suspended in serum-free medium. U87 cell suspensions ( $1.2 \times 10^4$  cells in 4  $\mu\text{L}$  serum-free medium) were injected intracranially to the right caudal diencephalon of nude mice (n = 6) [28–30].

A breast cancer brain metastasis (BCBM) mouse model with intracardiac injection of brain tropic breast cancer cells has been previously established at the lab [31,32]. Briefly, MDA-MB-231-BR cells (kindly provided by Dr. Steeg, NCI) were cultured in DMEM with 10% FBS, 1% L-Glutamine, and 1% penicillin-streptomycin at 37 °C with 5% CO<sub>2</sub>. Once 80% confluence was achieved, the cells were harvested and suspended in serum-free medium.  $2 \times 10^5$  MDA-MB-231-BR cells in 50  $\mu\text{L}$  serum-free medium were injected directly into the left ventricle of nude mice (n = 3) under ultrasound imaging guidance (Vevo LAZR, FUJIFILM VisualSonics, Inc. Toronto, Canada).

### 2.2 MRI acquisition and DCE MRI

Two weeks after tumor implantation, MRI was conducted. All MR imaging was performed on a Bruker 7T Biospec 70/30 USR scanner (Bruker Biospin, Rheinstetten, Germany). The mice were anesthetized in a chamber with 3% isoflurane, placed in a 30 cm horizontal bore magnet, and the tail vein was catheterized for bolus injection of Gd-DTPA (Magnevist; Bayer Healthcare) using a 27G butterfly. Animal respiration was monitored and maintained throughout MRI experimentation using a respiratory bulb. Anatomical T2-w images were acquired using a Rapid Imaging with Refocused Echoes (RARE) sequence (TR/TE: 2500/50 msec; Number of Scan Averages (NSA): 8; Echo Train Length (ETL): 8, Field of View (FOV): 22 mm  $\times$  22 mm; Slice Thickness (ST): 1 mm; scan time: 5 min 22 sec). Before DCE-MRI, high-resolution images were captured for  $T_1$  mapping by variable flip angles (TR/TE: 100/2.24 msec; NSA: 6; FOV: 22 mm  $\times$  22 mm; ST: 1 mm; Flip Angle (FA): 5, 10, 20, 35 degrees; scan time: 57 sec/FA). DCE-MRI was performed using a rapid  $T_1$ -w FLASH image sequence (TR/TE: 43/2.3 msec; FA: 30 degrees; FOV: 22 mm  $\times$  22 mm; NSA: 2; scan time: 6 min 57 sec) with dynamic images acquired before and after the bolus injection of Gd-DTPA (0.1 mmol/kg, i.v.) to ensure capture of Gd-DTPA kinetics. For each animal,

dynamic images of five consecutive slices were acquired were to cover the tumor region [32]. Lastly, T<sub>1</sub>-w contrast enhanced imaging was performed using a T<sub>1</sub>-w RARE sequence (TR/TE: 800/7 msec; ETL: 8; NSA: 8; FOV: 22 mm × 22 mm; scan time 2 min 33 sec). All anatomical imaging covered the region from the frontal lobe to the posterior fossa.

The acquired images were extracted in both raw Bruker 2dseq and DICOM file formats. An additional 3D Gaussian filter was used on DCE dynamic data. DCE images and variable flip angle T<sub>1</sub> series were co-registered with T2-w images to eliminate motion artifacts due to respiration. Homemade MATLAB R2020b scripts were developed for data processing and storage.

### 2.3 Construction of DCE MRI permeability parameters using PK models

Co-registered T<sub>1</sub> multiple flip angle images that were acquired at angles 5, 10, 20, and 35 were used to calculate T<sub>10</sub> maps using the method proposed in Brookes *et al.* [33]. The SI of each flip angle image is stacked into an array for each pixel. X coordinates were computed by dividing the SI at each pixel by tangent of the respective variable flip angle (VA).

$$X = \frac{SI}{\tan(VA)} \quad (1)$$

Similarly, Y coordinates were calculated by dividing the SI by sine of each angle.

$$Y = \frac{SI}{\sin(VA)} \quad (2)$$

These coordinates were then linearly fitted to quantity the slope (Sp). The T<sub>10</sub> values, tissue relaxation precontrast, at each pixel is estimated by:

$$T_{10} = -Tr/\log(Sp) \quad (3)$$

where Tr is the repetition time of the MR scan. These T<sub>1</sub> maps were used to generate CA concentration maps based on Brookes *et al.* [33] from the motion-corrected dynamic images. Dynamic SI was used to evaluate the CA concentration at each pixel. The equations involved were:

$$\frac{1}{T_1} = \frac{1}{T_{10}} + r_1 * C_t(t) \quad (4)$$

where T<sub>1</sub> is deducted from T<sub>10</sub> and which includes the presence of CA. r<sub>1</sub> is the relaxivity, which is 3.11 s<sup>-1</sup> mM<sup>-1</sup> for Gd-DPTA at 7T. The final C<sub>t</sub>(t) was determined from S(t), the SI of the dynamic time series, given by

$$S(t) = S_0 \frac{(1 - e^{-T_r/T_1}) \sin\theta}{1 - e^{-T_r/T_1 \cos\theta}} \quad (5)$$

where  $S_0$  is the initial single intensity of the dynamic time series at each pixel.  $\theta$  is the flip angle of the DCE MRI sequence. A population-based averaged AIF determined from literature was implemented to avoid poor AIF estimation and to enhance the reproducibility of PK parameters [18,20]. Here a bi-exponential AIF was implemented as AIFs fit well to a bi-exponential decay model as suggested by Cheng *et al.* [17]. The AIF was generated according to Eqn. 6.

$$AIF(t) = ae^{-c_1 t} + be^{-c_2 t} \quad (6)$$

where  $a$  and  $b$  are the coefficients determined from a population average of the AIF and  $c_1$  and  $c_2$  are the rates of decay of the AIF.  $c_1$  and  $c_2$  represent the uptake and washout of CA respectively. The Tofts model, Eqn. 7, and the Ex-Tofts model, Eqn. 8, were each applied to dynamic DCE data to estimate the kinetic parameters from CA concentration in the tissue and the AIF.

$$C_t(t) = K_{trans} \int_0^t C_p(\tau) e^{-K_{ep}(t-\tau)} d\tau \quad (7)$$

$$C_t(t) = V_p C_p(t) + K_{trans} \int_0^t C_p(\tau) e^{-K_{ep}(t-\tau)} d\tau \quad (8)$$

where  $K_{trans}$  is the transfer rate constant from the blood plasma to the EES,  $K_{ep}$  is the transfer rate constant from the EES to the blood plasma, and  $V_p$  is the fractional volume of blood plasma.  $C_t(t)$  is the concentration of CA in the tissue and  $C_p(t)$  is the concentration of CA in blood plasma (AIF) [13,14].  $V_e$  is the fractional EES volume that is the ratio of  $K_{trans}$  to  $K_{ep}$ . Here Tofts  $K_{trans}$ , Ex-Tofts  $K_{trans}$ , and Ex-Tofts  $V_p$  maps were generated and used for training and testing a convolutional neural network.

## 2.4 Convolutional neural network

In this study, the parameters are considered as a mapping problem between the dynamic time series and parameter maps. The CNN is trained to map the concentration of CA to the output. The estimated parameters from either the Tofts model or the Ex-Tofts model are processed as target images to the 24-layer CNN (Supplementary Fig. 1). The first convolutional layer applies 2D filters to each channel individually to extract low-level features. This was then followed by the two parallel pathways, local and global. The global pathway consists of 3 dilated convolutional layers each followed by a ReLU activation layer. The layers are dilated by factors of 2, 4 and 8, which captures the increase in receptive field size. This preserves the global structure and profile of the image. The local pathway consists of 3 non-dilated layers each of which are also followed by a ReLU activation layer. ReLU is applied to initiate nonlinearity into the mapping.

Zero-padding is applied to every convolutional operation to keep the spatial dimensions of the output the same as the input. The filter size of each convolutional layer is  $4 \times 4$ . The first convolutional layer has 128 filters, whose feature maps are then fed into the dual pathways

discussed above. Each layer in both the global and local pathways has 128 filters, which produce  $128 \times 128 \times 128$  feature maps each at the end. The pathways are concatenated to form a multiscale feature set. Following this, 4 fully connected layers of 1024, 512, 128 and 1 hidden node are used to derive the best feature combination that can accurately predict the outcome. Each convolutional layer was followed by a ReLU layer except for the last convolutional layer with one hidden node. Finally, a regression output layer with  $128 \times 128 \times 1$  node estimates the output maps. To maintain the spatial dimensions of the images, a regular convolution layer with  $1 \times 1$  filters is considered to be a fully connected layer.

The raw data from DCE MRI for each GBM animal was reshaped to have the temporal series as the third dimension and scan slice as the fourth dimension. Data sets were resized to  $128 \times 128 \times 40 \times 5$  by removing sequential images of the DCE scans involving more than 40 dynamic images. Each slice from the six animals were then stacked to create a single four-dimensional data set of size  $128 \times 128 \times 40 \times 30$ . Both the DCE dynamic images as well as the PK target maps were segmented to remove the skull and peripheral tissue surrounding the brain. DCE MRI data sets were batch normalized in each plane before feeding them into the network [34]. Training was performed using k-fold cross validation. To this end, imaging datasets from one mouse were isolated and held out for future testing. A neural network was then trained on the remaining five mice ( $n = 25$  slices) and was then tested with this isolated imaging dataset ( $n = 5$  slices). This process was then repeated de novo for a total of six times allowing each animal to serve as the testing data in separately trained networks. As we generated three separate PK target maps (Tofts Ktrans, Ex-Tofts Ktrans, and Ex-Tofts Vp), a total of 18 networks were trained. Among the image datasets left following isolation of the testing case, 80% were selected for training and 20% for validation. Selection of the validation data from training datasets was performed by sorting out a single random slice from each of the remaining five mice for each network. This was randomized for each of the networks to allow for rotation through the validation data in addition to rotation through training and testing data.

The networks were trained with a learning rate of  $10^{-4}$  and an L2-regularization of  $10^{-4}$  using the Adam optimizer [35]. A maximum of 600 epochs for a minibatch size of 20 was determined to prevent poor generalization when the validation loss stops improving. The validation checks were scheduled for every 2 iterations of training. Once each network was trained and the network parameters were determined, the test data set of the dynamic time series was fed into the network to directly predict the kinetic parameters. All of the code was implemented on MATLAB using the deep learning toolkit and an imported Keras library on a 3.7 GHz processor with 16 GB RAM. Each training session required an average time of 380 minutes.

A transfer study was then performed to assess if the GBM trained CNN could accurately predict PK maps for alternative brain tumors. Here, a total of 20 brain lesions detected in the three BCBM mice were implemented for testing. The DCE images of BCBM were preprocessed similar to the DCE images from the GBM study: reshaping of dynamic images to  $128 \times 128 \times 40 \times 5$ , segmentation to remove the skull and peripheral tissue surrounding the brain, and batch normalization. All six GBM mice ( $n = 30$  slices) were used as training data and fed into the aforementioned 24-layer CNN and trained using the same network

parameters as the GBM study. A total of three networks were trained, one for each PK parameter (Tofts Ktrans, Ex-Tofts Ktrans, and Ex-Tofts Vp). Once the networks were trained and the network parameters were determined, the preprocessed test data set of the dynamic time series for each brain metastasis case were fed into the network to directly predict the kinetic parameters.

## 2.5 Image processing

All image processing was performed in MATLAB using homemade scripts. Following testing of the proposed CNN, an ensemble of all networks was performed for each study. Intratumoral PK parameters from both the target PK parameter maps and the respective CNN maps were isolated for pixel-by-pixel comparisons. To this end, anatomical co-registered T<sub>1</sub>-CE images were used to manually mask the enhancing lesions and applied to corresponding PK parameter maps. For those that were non-enhancing on T<sub>1</sub>-CE images in the BCBM transfer study, co-registered T2-w images were used. Peripheral GBM tissue was defined as a single pixel towards the center of the lesions from the outer T<sub>1</sub>-CE lesion masks.

## 2.6 Statistical analysis

Statistical analysis was performed using Microsoft Excel (Microsoft Corporation, Redmond, WA, USA) and GraphPad Prism 9.0 (GraphPad Software, San Diego, CA, USA). Pixel-by-pixel comparisons of Ktrans and Vp values within tumor regions between the CNN and the PK models were conducted. Linear regression was applied to provide statistical correlation and significance. To compare the similarity between the CNN maps and the corresponding PK target maps, root mean squared error (RMSE) values of the brain tumor were calculated along with normalized RMSE (nRMSE) values based on target PK parameter standard distributions (SD). Bland-Altman plots were generated to assess general trends in the predictive capability of the proposed CNN.

## 3. Results

The Tofts Ktrans, Ex-Tofts Ktrans, and Ex-Tofts Vp generated maps were used as target maps to train the deep neural network. The time required to generate maps by the trained CNN was less than a few seconds with no human interference or additional data. The Tofts and Ex-Tofts model required additional MRI acquisitions for T<sub>1</sub> mapping thus increasing scan times and took longer to generate PK maps (Supplementary Table 1). In particular, the Ex-Tofts model typically took times up to five minutes for parameter map generation due to the need for non-linear least squares curve-fitting. These PK models necessitated additional data of CA arrival, T<sub>1</sub> mapping, complex curve-fitting algorithms, and knowledge of the AIF. For the k-fold cross validation GBM study, RMSE and nRMSE intratumoral values were calculated for each network to assess the performance of the proposed neural network across each network iteration (Table 1). As shown in Fig. 2, GBM lesions were identified on anatomic T2-w and T<sub>1</sub>-CE images. The hyperintense signal on T<sub>1</sub>-CE images resulted from high permeability of tumor vasculature. These tumors were used as testing cases in separately trained networks. Target maps of Tofts Ktrans, Ex-Tofts Ktrans, and Ex-Tofts Vp all exhibited intratumoral heterogeneity and high permeability parameter values in the tumor



region. Clearly, the corresponding CNN PK maps recapitulated this trend of intratumoral heterogeneity and increased permeability. Moreover, we applied a network trained solely with axial images to a coronal imaging dataset (Fig. 2, Case 3). The CNN successfully recapitulated coronal target PK parameter maps, suggesting this CNN approach is image orientation-independent.

To investigate if the CNN approach can decipher intratumoral heterogeneity, we conducted pixel-by-pixel comparisons between the CNN and the target PK models. Only the tumor region was considered following an ensemble of all networks for the GBM study ( $n = 30$  slices), containing a total of 7606 pixels. A significant linear correlation ( $p < 0.0001$ ) was found for each of the three target PK parameters and their corresponding CNN PK values (Fig. 3A). Similarly, all three PK parameters displayed low RMSE values less than the SD of the target PK parameters, indicating the ability of the CNN to generate PK values with minimal error. Furthermore, Bland-Altman plots indicated that the CNN did not show any trends in over-predicting or under-predicting the anticipated PK parameter values (Fig. 3B). We further investigated the predictive capabilities of the CNN for peripheral tumor tissue alone. Similar to the whole tumor region, a significant linear correlation ( $p < 0.0001$ ,  $n = 2236$ ) was found for each of the three target PK parameters and their corresponding CNN PK values (Supplementary Fig. 2A). RMSE values less than the SD was found for all PK parameters. Bland-Altman plots indicated that the CNN showed negligent over-predicting or under-predicting of the anticipated PK parameter values (Supplementary Fig. 2B).

Following training and testing the proposed CNN with GBM, we performed a transfer study with brain metastasis to assess the potential of the network for alternative brain tumors. A total of 20 BCBM lesions were identified across the 15 dynamic slices used in this study. Unlike the glioma model, multiple brain metastases including both contrast enhanced and non-enhanced lesions were commonly seen in the BCBM model, representing an excellent phenotype for testing the CNN approach for translation. Three networks, one for each target PK parameter, were trained solely with GBM datasets followed by testing with BCBM. Fig. 4 depicts three representative cases from individual BCBM mice. A small lesion was identified for Case 1 on anatomical images that exhibited increased vascular permeability on the target Tofts and Ex-Tofts PK maps. The CNN PK maps retained the small size and shape of the BCBM lesion while learning each corresponding PK parameter intratumoral values. Anatomical images for Case 2 revealed two tumors, one of which had only minimal enhancement on the T<sub>1</sub>-CE image (Fig. 4, arrow). Target PK parameter maps displayed increased K<sub>trans</sub> and V<sub>p</sub> values in the larger lesion, but lower values in the smaller lesion (arrow). In good agreement, the CNN PK maps revealed differential permeability between the two lesions. Similar to Case 2, Case 3 presented two lesions with differential vascular permeability, but with much smaller size than those of Case 2. Clearly, the CNN was able to recapitulate the small size and shape of the enhancing lesion and displayed low values of PK parameters in the minimally enhancing lesion.

Like the above glioma analysis, we conducted pixel-by-pixel comparisons for the BCBM. There were a total of 20 lesions identified across the DCE dynamic images ( $n = 15$  slices), 14 of which were enhancing while six of them were non-enhancing, indicating an intact BBB. Intratumoral pixel-by-pixel comparison revealed significant linear correlation ( $p <$

0.0001,  $n = 1148$  pixels) for each of the three target PK parameters and their corresponding CNN PK values (Fig. 5A). The RMSE values for the Tofts Ktrans and the Ex-Tofts Vp were found to be smaller than the target PK parameter SDs, whereas the RMSE value for the Ex-Tofts Ktrans was found to be slightly larger than the SD ( $nRMSE = 1.43$ ). Bland-Altman plots for all three PK parameters, particularly the Ex-Tofts Ktrans, exhibited a small positive bias (Fig. 5B).

#### 4. Discussion

In this study, we have successfully developed a deep learning-based CNN model to generate the PK parameters for DCE MRI. CNNs are often implemented when working with images and are the most commonly used networks for pattern recognition tasks [36]. Hence, as generation of PK parameters is considered as a mapping problem to train a deep neural network to recognize patterns of increased heterogeneous intratumoral PK parameters from source DCE images, a CNN was chosen as an ideal network for this study. The specific CNN methodology as used in this study has previously been shown to yield accurate PK parameters directly from DCE images in different brain regions of stroke patients without conventional PK modeling. Hence, we hypothesized this CNN could be translated to small animal brain tumor research studies. Generative adversarial networks (GANs) have been gaining popularity in medical image processing as a more sophisticated deep learning method in which two networks compete against each other and hence might serve as a potential network for this application in future studies [36,37]. Nevertheless, our results show a good match for both Ktrans and Vp maps generated between the target PK parameter maps and the respective CNN PK parameter maps for brain tumors. Importantly, the CNN PK maps were shown to successfully recapitulate intratumoral heterogeneity and increased permeability in accordance with their target PK model parameter maps. The CNN approach to directly generate the PK maps from DCE dynamic images is time efficient (within a few seconds) and requires no human interference or additional data, whereas conventional PK modeling is much more time consuming and requires additional information including CA arrival,  $T_1$  mapping, and the AIF alongside complex curve-fitting algorithms.

K-fold cross validation is commonly implemented in deep learning applications to assess the performance of the neural network through cycling training and testing datasets [27,38,39]. This methodology ensures that the network can be transferred to alternative testing cases of variable phenotypes and that the network is avoiding overfitting of the training data through increasing the amount of testing data. Here we trained and tested a total of 21 networks, 18 for the GBM study and 3 for the brain metastasis transfer study. In the k-fold cross validation GBM study, similar RMSE and nRMSE values were found for each respective PK parameter (Tofts Ktrans, Ex-Tofts Ktrans, and Ex-Tofts Vp) across each network demonstrating the power of the deep learning approach to decipher intertumor variation for each testing case with high accuracy (Table 1). In particular, the target Ex-Tofts Ktrans and CNN produced consistently low RMSE values below the target parameter SD ( $nRMSE < 1$ ). Further quantification of the performance of these networks in the GBM study involved linear regression analysis for correlation and statistical significance, RMSE, and Bland-Altman plot analysis following intratumoral ensembles of the networks. For the GBM study, we found significant linear correlations ( $p < 0.0001$ ), low RMSEs, and negligible

over/under-prediction of the CNN for all three target PK parameters in both intratumoral and peripheral tumor regions (Fig. 3, Supplementary Fig. 2). Clearly the proposed CNN has the ability to generate PK parameter maps structurally similar to its target PK maps. Importantly, the CNN has the ability to be transferred not only between different PK parameters, but also between different PK models, i.e., the Tofts and Ex-Tofts models.

In line with the GBM study, significant linear correlations ( $p < 0.0001$ ) were evidenced for all three PK parameters in the BCBM transfer study. The enhanced correlation coefficients for the BCBM transfer study might be a result of increasing the training datasets through the inclusion of an additional GBM imaging dataset. Hence, we anticipate that incorporation of additional training datasets will lead to more robust predictive capabilities of the network. Despite training the networks solely with large GBM images, the CNN was able to recapitulate the smaller size of BCBM tumors (Fig. 4). Moreover, the CNN accurately identified the PK parameter values in BCBMs with differential permeability as well as those with cerebrospinal fluid (CSF) enhancement (Fig. 4). In addition to intertumor variation, the CNN was capable of depicting intratumoral vascular heterogeneity in brain metastases as evidenced with the pixel-by-pixel analysis (Fig. 5) consistent with the finding in GBM (Fig. 3). Bland-Altman plot analysis revealed that the CNN on average might slightly over-predict the intratumoral PK values for the BCBM transfer study (Fig. 5). GBM is notoriously highly angiogenic with the presence of leaky microvessels and hence generate large PK permeability parameter values. On the contrary, brain metastases, particularly smaller lesions, often retain intact blood-tumor barriers (BTBs) and exhibit no enhancement on T<sub>1</sub>-CE images and low permeability on PK maps, as shown in Fig. 4 [32]. Hence, as we trained the networks with high permeability GBM datasets, we anticipate this to be a driving force for the slight CNN over-prediction of PK parameter values. Nevertheless, the results from the BCBM transfer study clearly indicate that the CNN has the ability to translate to alternative brain tumor phenotypes differing in size, shape, and/or permeability.

In general, deep learning and machine learning algorithms require huge amounts of data to perform efficiently upon training [40]. With limited availability of animal data in this study, there is a higher risk of overfitting the data, which can cause poor generalization and contribute to crude predictions. To solve such complications, the algorithm requires additional data to converge to a general case. Recent studies have shown the impact of augmented data in solving overfitting problems [41,42]. However, this approach of data augmentation was computationally costly and complex on this project as the DCE data trained was a complex time-dependent series of images. Hence, we proceeded with no additional data augmented to train the network. Despite a small number of training data for both the GBM study ( $n = 25$  slices) and the brain metastasis transfer study ( $n = 30$  slices), our results indicate that the proposed neural network can still efficiently recapitulate the tumor size, shape, and PK permeability parameters in both primary and metastatic brain tumors while avoiding overfitting of the data as evidenced through its translatability to alternative brain tumor phenotypes. This is likely attributable to the fact that each of these training ‘slices’ involved multiple complex dynamic images with thousands of pixels per image for the network to learn from.

## 5. Conclusions

In summary, we have successfully deployed the Tofts model and the Ex-Tofts model as well as a deep learning-based CNN to study vascular permeability in small animal brain tumors. Results and observations from the CNN infer that this deep learning approach could perform as precisely as the conventional PK models. Importantly, the CNN approach requires limited data without human intervention and can be completed with much less time. Future studies by training and testing the system with more data and including additional glioma models with differential phenotypes of tumor aggressiveness and angiogenesis will be needed to further establish its utility. Furthermore, implementation of an accurate AIF measurement in these small animals in a case-by-case basis prior to CNN training might enhance the accuracy of the produced conventional PK and CNN maps by taking into account individual variation. We anticipate that the proposed deep learning-based CNN will serve as a useful surrogate for small animal brain tumor research of vascular PK parameters.

## Supplementary Material

Refer to Web version on PubMed Central for supplementary material.

## Acknowledgment

We are grateful to Jared Weis, Biomedical Engineering at Wake Forest, Umit Topaloglu, Cancer Biology at Wake Forest, and Hannah Dailey, Mechanical Engineering and Mechanics at Lehigh University, for valuable input and collegial support.

## Funding

This research has been supported in part by NIH/NCI R01 CA194578 and Wake Forest Comprehensive Cancer Center under Grant P30 CA01219740.

## Abbreviations

<b>AIF</b>	arterial input function
<b>BBB</b>	blood-brain barrier
<b>BCBM</b>	breast cancer brain metastasis
<b>BTB</b>	blood-tumor barrier
<b>CA</b>	contrast agent
<b>CNN</b>	convolutional neural network
<b>CSF</b>	cerebrospinal fluid
<b>DCE MRI</b>	dynamic contrast-enhanced MRI
<b>DMEM</b>	Dulbecco's modified Eagle's medium
<b>EES</b>	extravascular extracellular space
<b>ETL</b>	echo train length

<b>Ex-Tofts</b>	extended Tofts
<b>FA</b>	flip angle
<b>FOV</b>	field of view
<b>GBM</b>	glioblastoma multiforme
<b>Kep</b>	flux rate constant
<b>Ktrans</b>	volume transfer coefficient
<b>nRMSE</b>	normalized root mean squared error
<b>NSA</b>	number of scan averages
<b>PK</b>	pharmacokinetic
<b>RARE</b>	rapid imaging with refocused echoes
<b>RMSE</b>	root mean squared error
<b>SD</b>	standard distribution
<b>SI</b>	signal intensity
<b>Sp</b>	slope
<b>ST</b>	slice thickness
<b>T<sub>1</sub>-w</b>	T <sub>1</sub> -weighted
<b>VA</b>	variable flip angle
<b>Ve</b>	fractional volume of the EES
<b>VIF</b>	vascular input function
<b>Vp</b>	fractional volume of the blood plasma.

## References

- [1]. Kroll RA, Neuwelt EA. Outwitting the blood-brain barrier for therapeutic purposes: osmotic opening and other means. *Neurosurgery*. 1998; 42: 1083–1100. [PubMed: 9588554]
- [2]. Gilbertson RJ, Rich JN. Making a tumour's bed: glioblastoma stem cells and the vascular niche. *Nature Reviews Cancer*. 2007; 7: 733–736. [PubMed: 17882276]
- [3]. Jain RK, di Tomaso E, Duda DG, Loeffler JS, Sorensen AG, Batchelor TT. Angiogenesis in brain tumours. *Nature Reviews Neuroscience*. 2007; 8: 610–622. [PubMed: 17643088]
- [4]. Steeg PS. The blood-tumour barrier in cancer biology and therapy. *Nature Reviews Clinical Oncology*. 2021; 18: 696–714.
- [5]. Zhang L, Zhang Z, Mason RP, Sarkaria JN, Zhao D. Convertible MRI contrast: Sensing the delivery and release of anti-glioma nano-drugs. *Scientific Reports*. 2015; 5: 9874. [PubMed: 25962872]
- [6]. Nielsen T, Wittenborn T, Horsman MR. Dynamic Contrast-Enhanced Magnetic Resonance Imaging (DCE-MRI) in Preclinical Studies of Antivascular Treatments. *Pharmaceutics*. 2012; 4: 563–589. [PubMed: 24300371]

- [7]. Türkbey B, Thomasson D, Pang Y, Bernardo M, Choyke PL. The role of dynamic contrast-enhanced MRI in cancer diagnosis and treatment. *Diagnostic and Interventional Radiology*. 2010; 16: 186–192. [PubMed: 19885783]
- [8]. Evelhoch JL. Key factors in the acquisition of contrast kinetic data for oncology. *Journal of Magnetic Resonance Imaging*. 1999; 10: 254–259. [PubMed: 10508284]
- [9]. Gerales CFGC, Laurent S. Classification and basic properties of contrast agents for magnetic resonance imaging. *Contrast Media & Molecular Imaging*. 2009; 4: 1–23. [PubMed: 19156706]
- [10]. Heye AK, Thrippleton MJ, Armitage PA, Valdés Hernández MDC, Makin SD, Glatz A, et al. Tracer kinetic modelling for DCE-MRI quantification of subtle blood-brain barrier permeability. *NeuroImage*. 2016; 125: 446–455. [PubMed: 26477653]
- [11]. Sourbron SP, Buckley DL. Classic models for dynamic contrast-enhanced MRI. *NMR in Biomedicine*. 2013; 26: 1004–1027. [PubMed: 23674304]
- [12]. Brix G, Semmler W, Port R, Schad LR, Layer G, Lorenz WJ. Pharmacokinetic parameters in CNS Gd-DTPA enhanced MR imaging. *Journal of Computer Assisted Tomography*. 1991; 15: 621–628. [PubMed: 2061479]
- [13]. Tofts PS. Modeling tracer kinetics in dynamic Gd-DTPA MR imaging. *Journal of Magnetic Resonance Imaging*. 1997; 7: 91–101. [PubMed: 9039598]
- [14]. Tofts PS, Brix G, Buckley DL, Evelhoch JL, Henderson E, Knopp MV, et al. Estimating kinetic parameters from dynamic contrast-enhanced T<sub>1</sub>-weighted MRI of a diffusable tracer: standardized quantities and symbols. *Journal of Magnetic Resonance Imaging*. 1999; 10: 223–232. [PubMed: 10508281]
- [15]. Dujardin MI, Sourbron SP, Chaskis C, Verellen D, Stadnik T, de Mey J, et al. Quantification of cerebral tumour blood flow and permeability with T<sub>1</sub>-weighted dynamic contrast enhanced MRI: a feasibility study. *Journal of Neuroradiology*. 2012; 39: 227–235. [PubMed: 21840059]
- [16]. Calamante F Arterial input function in perfusion MRI: a comprehensive review. *Progress in Nuclear Magnetic Resonance Spectroscopy*. 2013; 74: 1–32. [PubMed: 24083460]
- [17]. Cheng HM. T<sub>1</sub> measurement of flowing blood and arterial input function determination for quantitative 3D T<sub>1</sub>-weighted DCE-MRI. *Journal of Magnetic Resonance Imaging*. 2007; 25: 1073–1078. [PubMed: 17410576]
- [18]. McGrath DM, Bradley DP, Tessier JL, Lacey T, Taylor CJ, Parker GJM. Comparison of model-based arterial input functions for dynamic contrast-enhanced MRI in tumor bearing rats. *Magnetic Resonance in Medicine*. 2009; 61:1173–1184. [PubMed: 19253360]
- [19]. Cheng HM. Investigation and optimization of parameter accuracy in dynamic contrast-enhanced MRI. *Journal of Magnetic Resonance Imaging*. 2008; 28: 736–743. [PubMed: 18777534]
- [20]. Parker GJM, Roberts C, Macdonald A, Buonaccorsi GA, Cheung S, Buckley DL, et al. Experimentally-derived functional form for a population-averaged high-temporal-resolution arterial input function for dynamic contrast-enhanced MRI. *Magnetic Resonance in Medicine*. 2006; 56: 993–1000. [PubMed: 17036301]
- [21]. Morrison DD. Methods for nonlinear least squares problems and convergence proofs. *JPL Seminar Proceedings*. 1960; 1–9.
- [22]. Wang S, Summers RM. Machine learning and radiology. *Medical Image Analysis*. 2012; 16: 933–951. [PubMed: 22465077]
- [23]. Lo SB, Lou SA, Lin JS, Freedman MT, Chien MV, Mun SK. Artificial convolution neural network techniques and applications for lung nodule detection. *IEEE Transactions on Medical Imaging*. 1995; 14: 711–718. [PubMed: 18215875]
- [24]. Lundervold AS, Lundervold A. An overview of deep learning in medical imaging focusing on MRI. *Zeitschrift Fur Medizinische Physik*. 2019; 29: 102–127. [PubMed: 30553609]
- [25]. Choi KS, You S, Han Y, Ye JC, Jeong B, Choi SH. Improving the Reliability of Pharmacokinetic Parameters at Dynamic Contrast-enhanced MRI in Astrocytomas: a Deep Learning Approach. *Radiology*. 2020; 297: 178–188. [PubMed: 32749203]
- [26]. Nalepa J, Ribalta Lorenzo P, Marcinkiewicz M, Bobek-Billewicz B, Wawrzyniak P, Walczak M, et al. Fully-automated deep learning-powered system for DCE-MRI analysis of brain tumors. *Artificial Intelligence in Medicine*. 2020; 102: 101769. [PubMed: 31980106]

- [27]. Ulas C, Das D, Thrippleton MJ, Valdés Hernández MDC, Armitage PA, Makin SD, et al. Convolutional Neural Networks for Direct Inference of Pharmacokinetic Parameters: Application to Stroke Dynamic Contrast-Enhanced MRI. *Frontiers in Neurology*. 2018; 9: 1147. [PubMed: 30671015]
- [28]. Zhao D, Stafford JH, Zhou H, Thorpe PE. Near-infrared Optical Imaging of Exposed Phosphatidylserine in a Mouse Glioma Model. *Translational Oncology*. 2011; 4: 355–364. [PubMed: 22191000]
- [29]. Zhang L, Habib AA, Zhao D. Phosphatidylserine-targeted liposome for enhanced glioma-selective imaging. *Oncotarget*. 2016; 7: 38693–38706. [PubMed: 27231848]
- [30]. Wang L, Habib AA, Mintz A, Li KC, Zhao D. Phosphatidylserine-Targeted Nanotheranostics for Brain Tumor Imaging and Therapeutic Potential. *Molecular Imaging*. 2017; 16: 1536012117708722. [PubMed: 28654387]
- [31]. Zhou H, Chen M, Zhao D. Longitudinal MRI evaluation of intracranial development and vascular characteristics of breast cancer brain metastases in a mouse model. *PLoS ONE*. 2013; 8: e62238. [PubMed: 23638013]
- [32]. Crowe W, Wang L, Zhang Z, Varagic J, Bourland JD, Chan MD, et al. MRI evaluation of the effects of whole brain radiotherapy on breast cancer brain metastasis. *International Journal of Radiation Biology*. 2019; 95: 338–346. [PubMed: 30499763]
- [33]. Brookes JA, Redpath TW, Gilbert FJ, Murray AD, Staff RT. Accuracy of T<sub>1</sub> measurement in dynamic contrast-enhanced breast MRI using two- and three-dimensional variable flip angle fast low-angle shot. *Journal of Magnetic Resonance Imaging*. 1999; 9: 163–171. [PubMed: 10077009]
- [34]. Ioffe S, Szegedy C. Batch Normalization: Accelerating Deep Network Training by Reducing Internal Covariate Shift. *Proceedings of Machine Learning Research*. 2015; 37: 448–456.
- [35]. Kingma DP, Ba JL. Adam: A Method for Stochastic Optimization. *International Conference on Learning Representations*. San Diego. 2015. arXiv: 1412.6980. 2015.
- [36]. Chan H, Samala RK, Hadjiiski LM, Zhou C. Deep Learning in Medical Image Analysis. *Advances in Experimental Medicine and Biology*. 2020; 89: 3–21.
- [37]. Lan L, You L, Zhang Z, Fan Z, Zhao W, Zeng N, et al. Generative Adversarial Networks and Its Applications in Biomedical Informatics. *Front Public Health*. 2020; 8: 164. [PubMed: 32478029]
- [38]. Su P, Guo S, Roys S, Maier F, Bhat H, Melhem ER, et al. Transcranial MR Imaging-Guided Focused Ultrasound Interventions Using Deep Learning Synthesized CT. *American Journal of Neuroradiology*. 2020; 41: 1841–1848. [PubMed: 32883668]
- [39]. Holbrook MD, Blocker SJ, Mowery YM, Badea A, Qi Y, Xu ES, et al. MRI-Based Deep Learning Segmentation and Radiomics of Sarcoma in Mice. *Tomography*. 2020; 6: 23–33. [PubMed: 32280747]
- [40]. Yamashita R, Nishio M, Do RKG, Togashi K. Convolutional neural networks: an overview and application in radiology. *Insights into Imaging*. 2018; 9: 611–629. [PubMed: 29934920]
- [41]. Alber M, Buganza Tepole A, Cannon WR, De S, Dura-Bernal S, Garikipati K, et al. Integrating machine learning and multiscale modeling—perspectives, challenges, and opportunities in the biological, biomedical, and behavioral sciences. *NPJ Digital Medicine*. 2019; 2: 115. [PubMed: 31799423]
- [42]. Gu J, Wang Z, Kuen J, Ma L, Shahroudy A, Shuai B, et al. Recent advances in convolutional neural networks. *Pattern Recognition*. 2018; 77: 354–377.

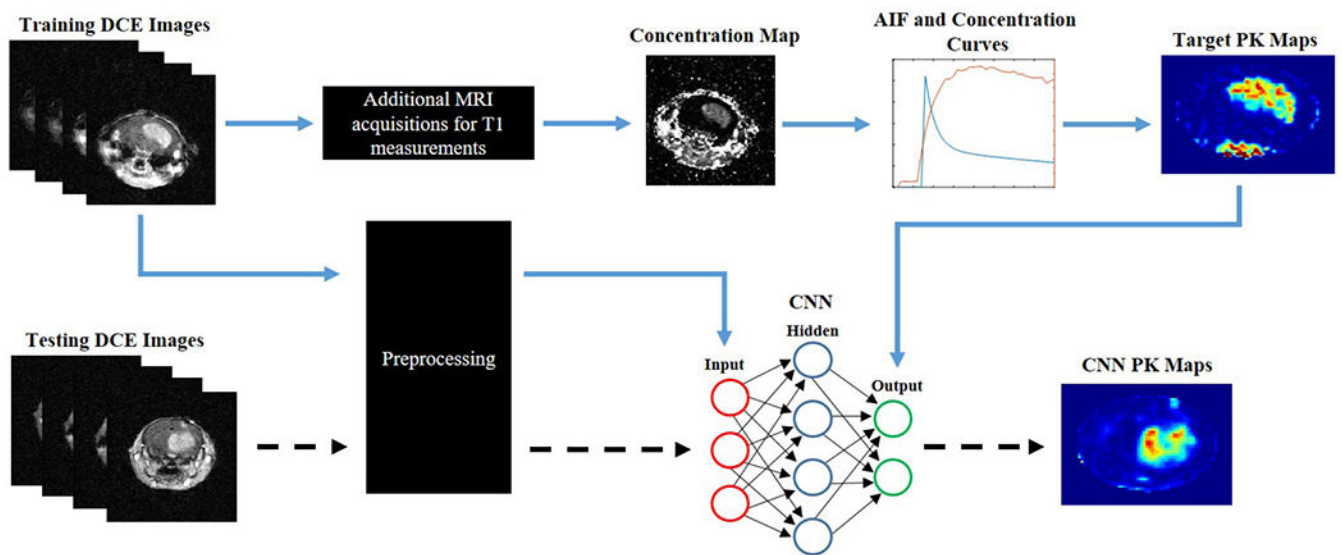


**Fig. 1. Pipeline and workflow of this project.**

Conventional PK modeling is applied to DCE dynamic images to generate target PK maps. Source DCE dynamic images and target PK maps are fed into the 24-layer CNN for training (blue arrows). An independent testing DCE dynamic imaging dataset can be fed directly into the CNN to generate CNN PK maps following training of the neural network (dashed arrows). Preprocessing of the DCE dynamic images involved reshaping, segmentation, and batch normalization. The neural network can directly predict the PK maps with the DCE time series alone. In contrast, conventional PK modeling requires manual CA arrival identification, additional MRI acquisitions for T1 measurements, complex curve-fitting, as well as the knowledge of the AIF along with the DCE time series in order to estimate these kinetic parameters.



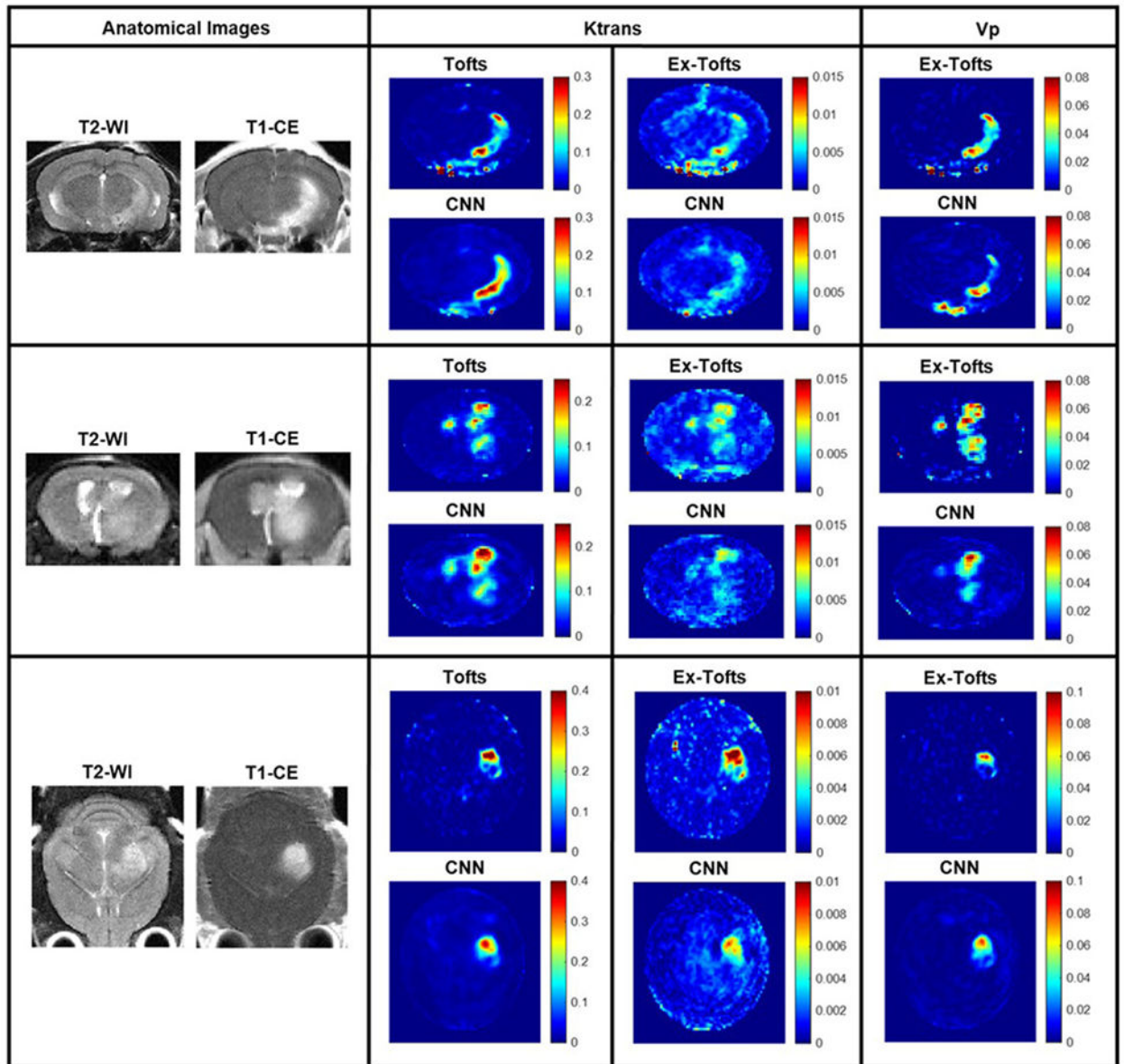


**Fig. 2. GBM study.**

Three cases from the GBM study with permeable lesions. Anatomical T2-w and T<sub>1</sub>-CE images were provided for reference. Tofts Ktrans, Ex-Tofts Ktrans, and Ex-Tofts Vp target maps as well as their corresponding CNN PK maps all displayed intratumoral heterogeneity and increased permeability.

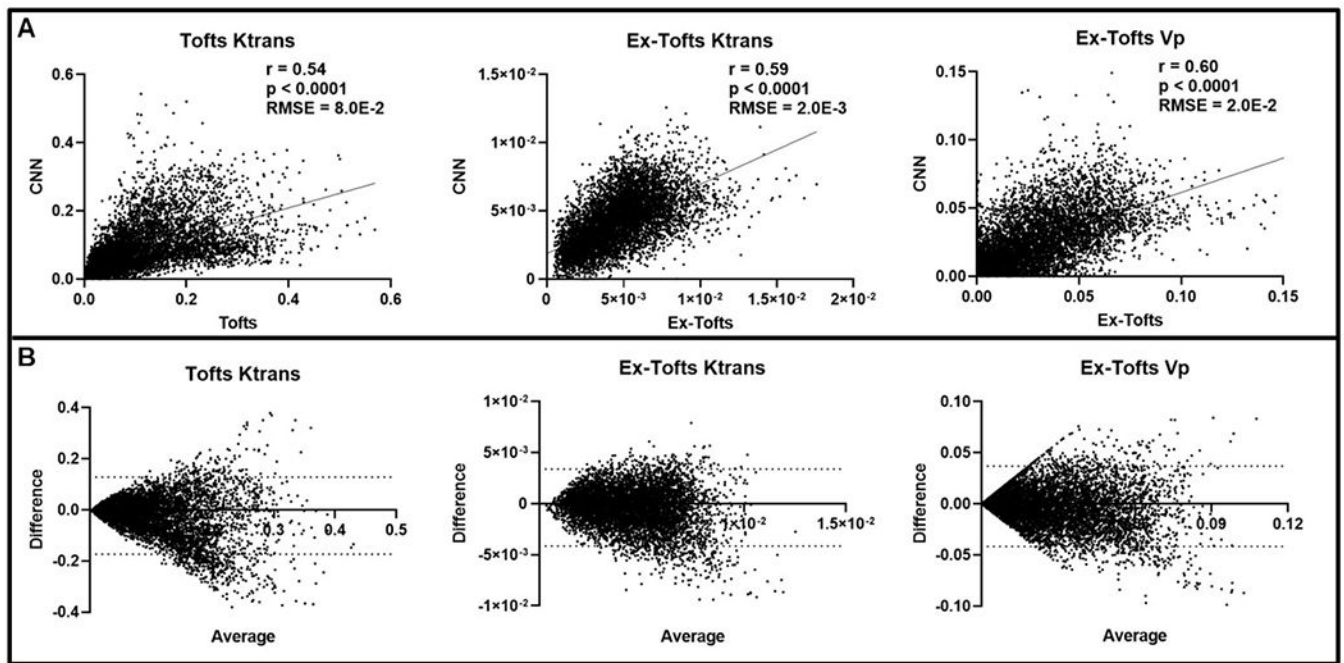


**Fig. 3. Intratumoral ensemble analysis of GBM.**

(A) Pixel-by-pixel data ( $n = 7606$ ) of intratumoral regions were plotted, revealing a significant linear correlation for Ktrans and Vp between CNN and target PK models ( $p < 0.0001$ ). Low RMSEs were found between the target PK models and the CNN for all three parameters ( $RMSE < \text{Target PK parameter SD}$ ). (B) Bland-Altman plots of PK parameters were generated with dashed lines corresponding to the upper and lower 95% confidence intervals.

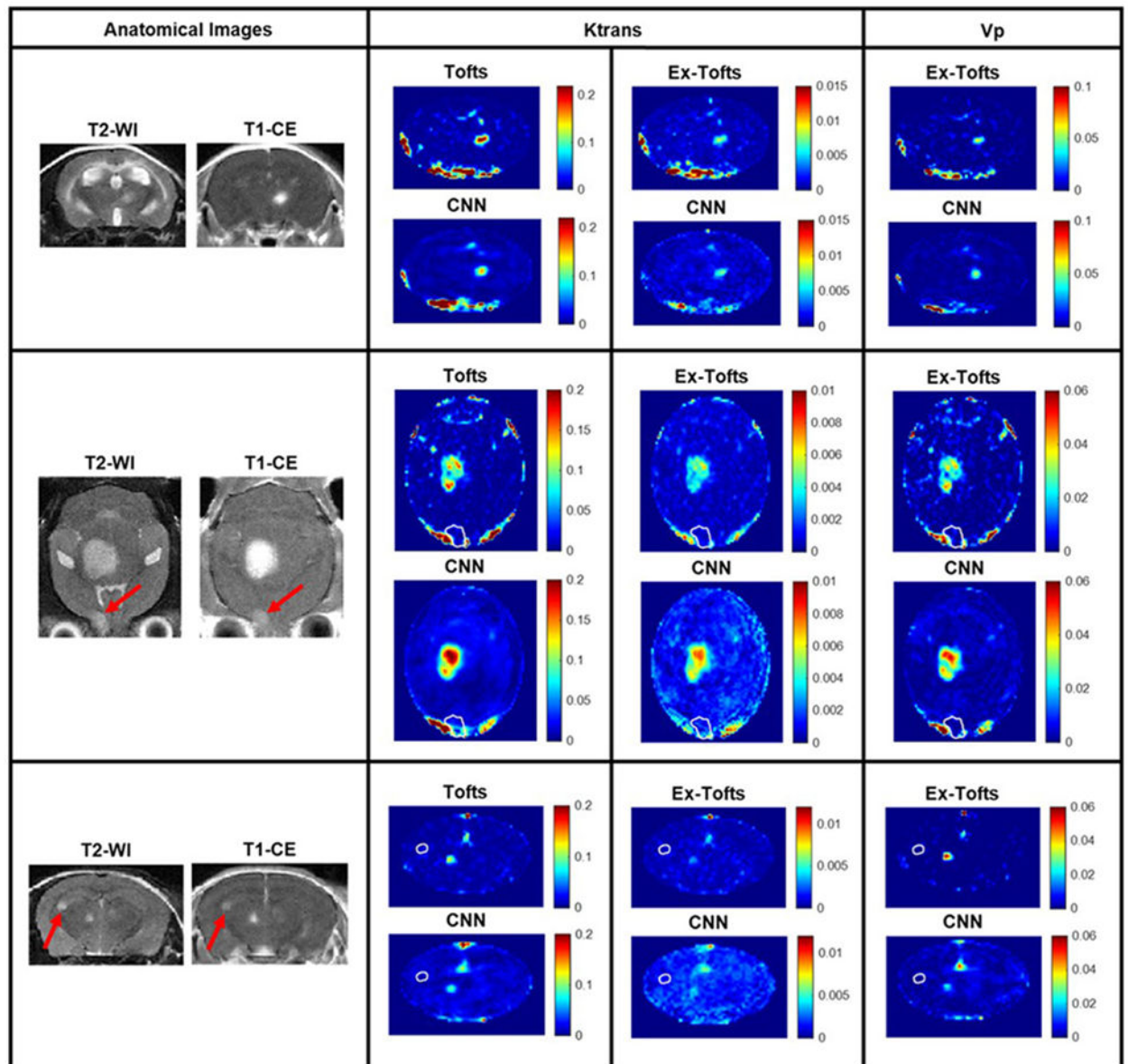


**Fig. 4. Brain metastasis transfer study.**

MR imaging investigation of the brain metastasis transfer study revealed lesions with differing size, shape, and permeability. Tofts Ktrans, Ex-Tofts Ktrans, and Ex-Tofts Vp target maps as well as their corresponding CNN PK maps were depicted. The T2-w detectable edge of the lesions in Case 2 and 3 that exhibited lower permeability (arrows) were superimposed as a white contour on the PK maps.

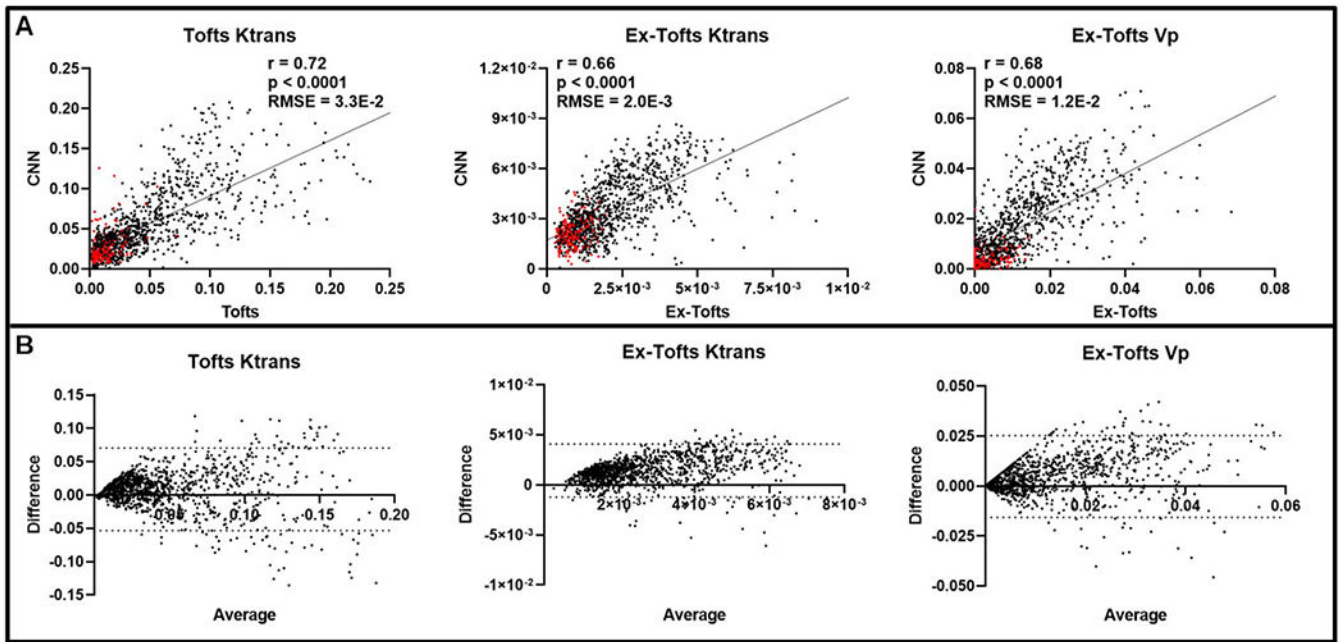


**Fig. 5. Intratumoral ensemble analysis of brain metastases.**

(A) Pixel-by-pixel data ( $n = 1148$ ) of intratumoral regions were plotted that revealed significant linear correlations between the CNN and target PK parameters ( $p < 0.0001$ ). Non-enhancing lesions ( $n = 187$ ) Ktrans and Vp values are shown in red. RMSEs for all PK parameters were calculated and displayed. (B) Bland-Altman plots of PK parameters were generated with dashed lines corresponding to the upper and lower 95% confidence intervals.

**Table 1.**

Predictive performance of CNN in k-fold cross validation GBM study.

Target PK model	Metric	Network 1	Network 2	Network 3	Network 4	Network 5	Network 6
Tofts Ktrans	RMSE	$8.60 \times 10^{-2}$	$8.73 \times 10^{-2}$	$2.37 \times 10^{-2}$	$4.34 \times 10^{-2}$	$1.34 \times 10^{-1}$	$7.05 \times 10^{-2}$
	nRMSE	1.28	1.04	1.02	0.83	1.26	0.76
Ex-Tofts Ktrans	RMSE	$1.87 \times 10^{-3}$	$2.24 \times 10^{-3}$	$1.50 \times 10^{-3}$	$1.88 \times 10^{-3}$	$1.84 \times 10^{-3}$	$2.31 \times 10^{-3}$
	nRMSE	0.80	0.95	0.86	0.94	0.97	0.93
Ex-Tofts Vp	RMSE	$1.72 \times 10^{-2}$	$2.36 \times 10^{-2}$	$1.58 \times 10^{-2}$	$1.88 \times 10^{-2}$	$2.04 \times 10^{-2}$	$2.27 \times 10^{-2}$
	nRMSE	0.86	0.81	1.04	0.90	0.81	1.38